

## New TeV-emitting BL Lac candidates from the eROSITA X-ray survey

CASSIDY METZGER <sup>1</sup>, ANDREA GOKUS <sup>1</sup> AND MANEL ERRANDO <sup>1</sup>

<sup>1</sup>*Department of Physics & McDonnell Center for the Space Sciences, Washington University in St. Louis, One Brookings Drive, St. Louis, MO 63130, USA*

### ABSTRACT

TeV-emitting BL Lac type blazars represent the extreme end of the blazar population. They are characterized by relatively weak jets and radiatively inefficient accretion disks. Particles accelerated in these jets experience fewer radiative losses, allowing them to reach energies beyond the TeV scale and produce TeV gamma-ray emission. The study of TeV blazars is constrained by the limited number of known sources in this category. Currently, only 56 high synchrotron-peaked BL Lacs have been detected at energies above 0.1 TeV. Searches for TeV emission from BL Lacs typically target sources with bright X-ray emission and a synchrotron peak at or above 1 keV. The recently released eRASS1 catalog by the eROSITA collaboration, which covers half of the sky, represents the deepest X-ray survey in the soft X-ray band to date. Utilizing the eROSITA survey, combined with infrared data from WISE and archival radio observations, we have identified 135 TeV-emitting blazar candidates. Our search introduces selection criteria based on the radio to infrared that remove quasar-like objects that have similar infrared spectra and X-ray fluxes as TeV-emitting BL Lacs. In our search, we find 26 objects that had not been detected in the ROSAT X-ray survey and 20 that have not been previously associated with blazars. The candidates resulting from our search are suitable for follow-up observations with currently operating imaging atmospheric Cherenkov telescopes, as well as future facilities like the CTAO Observatory.

*Keywords:* Blazars; BL Lacertae objects; Relativistic jets; Gamma-ray telescopes; X-ray surveys; Infrared sources

### 1. INTRODUCTION

Active galactic nuclei (AGN) are observed to launch relativistic jets powered by accretion onto a central supermassive black hole (e.g., see the recent review by Blandford et al. 2019). These collimated streams of matter and radiation occur in approximately 10% of AGN (Kellermann et al. 1989; Urry & Padovani 1995; Ivezić et al. 2002). The prevailing understanding of the physical structure of an AGN is that they consist of a central supermassive black hole ( $> 10^6 M_{\odot}$ ) with a surrounding accretion disk that emits ultraviolet and soft X-ray radiation. A warped ring of gas and dust, often depicted as a torus, encircles the accretion disk and obscures UV and optical radiation when viewed edge-on. Relativistic jets are launched perpendicular to the plane of the

accretion disk and can be seen across all wavelengths. A unified view of AGN proposed by Urry & Padovani (1995) posits that the various classes of AGN actually represent different perspectives of the same underlying object, depending on the observer's line of sight. Blazars exhibit the most extreme properties of all AGN. They are objects that we observe from a very small viewing angle, that is, with their jets pointed toward us, and exhibit large-amplitude flux variability across the electromagnetic spectrum. Their spectral-energy distribution (SED) typically has two distinct parts: a broad synchrotron component at lower energies and a second high-energy component that can extend into the gamma-ray band. In flat-spectrum radio quasars (FSRQs) and low-frequency peaked BL Lac-type blazars, the synchrotron peak typically appears in the infrared to UV wavelengths. However, in high-frequency peaked BL Lac-type blazars (HBLs), the synchrotron peak is located in the X-ray region ( $\nu_{\text{peak}} \geq 10^{15}$ ) (Padovani & Giommi 1995). The second component is attributed to

inverse Compton scattering, and in HBLs it can extend from X-rays to TeV gamma rays.

The high-energy component of the SED of some HBLs peaks beyond 10 TeV. These objects are often labeled extreme high-frequency peaked BL Lacs (eHBLs, Costamante et al. 2001; Bonnoli et al. 2015), and their emission challenges standard synchrotron self-Compton models for BL Lacs (Costamante et al. 2018). These BL Lacs with radiative output peaking in the TeV band have interesting implications for the study of jet phenomenology, particle acceleration, and production of ultra-high-energy cosmic rays and neutrinos, and can be used as probes of extragalactic background light (Aharonian et al. 2006; Mazin & Raue 2007; Biteau & Williams 2015) and cosmic magnetic fields (Neronov & Vovk 2010; Chen et al. 2015; Finke et al. 2015; Archambault et al. 2017; Acciari et al. 2023; Aharonian et al. 2023). However, due to the limited sensitivity and survey capabilities of TeV observatories (Aharonian et al. 2008; Sitarek 2022; Errando & Saito 2023), the number of eHBLs currently identified and characterized ranges from one to two dozen (Biteau et al. 2020).

The population of known gamma-ray-emitting blazars remains notably incomplete. The *Fermi*-LAT all-sky blazar survey is only complete at energy fluxes  $> 3 \times 10^{-12}$  erg cm $^{-2}$  s $^{-1}$  (Marcotulli et al. 2020), despite the LAT being able to significantly detect sources an order of magnitude fainter. Traditionally, blazars are identified as compact flat-spectrum radio sources with a continuum-dominated optical counterpart. Other characteristics, such as a point-like X-ray counterpart, detection of gamma-ray emission, optical polarization, or flux variability across radio, optical, or X-ray bands, further substantiate a blazar identification. Searches for new TeV-emitting blazars typically follow TeV flux predictions based on radio, optical and X-ray surveys (e.g., Costamante & Ghisellini 2002; Giommi et al. 2005). However, these searches are often limited by incomplete coverage of surveys at these wavelengths or by source confusion. Examples of these limitations are the growing number of blazars that have been serendipitously detected at low galactic latitudes in the GeV band (e.g., Mukherjee et al. 2000; Vandenbroucke et al. 2010; Kara et al. 2012) and at TeV energies (e.g., H. E. S. S. Collaboration et al. 2011; Archambault et al. 2013). These blazars do not appear in conventional blazar catalogs because optical and X-ray point source catalogs tend to be incomplete at low Galactic latitudes or exclude the Galactic plane altogether (e.g., Healey et al. 2008; Massaro et al. 2009). Recent efforts have aimed to identify new TeV-peaked blazar candidates using deeper and more complete radio, infrared, optical, and X-ray cata-

logs (e.g., Massaro et al. 2013; Costamante 2020) with the goal of observing and potentially detecting such candidates with ground-based gamma-ray observatories.

In this paper, we use the eRASS1 X-ray survey of the *eROSITA* mission (Merloni et al. 2024) to identify new TeV-emitting BL Lac candidates. The eRASS1 catalog covers the western galactic hemisphere (half of the sky) in the 0.2–2.3 keV energy range with a deeper sensitivity than any previous wide X-ray survey, resulting in a source density of  $\sim 45$  deg $^{-2}$ , more than an order of magnitude higher than the *ROSAT* 2RXS catalog (Boller et al. 2016).

To identify new candidate TeV-emitting BL Lacs we select infrared sources in the WISEA catalog (Wright et al. 2010; Mainzer et al. 2011) that occupy the region in the *WISE* color-color diagram where gamma-ray blazars are found (Massaro et al. 2012) and cross-match them with their X-ray counterparts in the *eROSITA* eRASS1 survey to select objects with a luminous synchrotron component peaking in the X-ray band.

## 2. TEV-EMITTING BL LAC-TYPE BLAZARS

The first step in our search for new candidate TeV-emitting HBLs is to establish the infrared and X-ray properties of known examples of this source class. BL Lac-type blazars are the most numerous class of extragalactic sources detected at TeV energies, with 68 currently detected (TeVcat<sup>1</sup>, Wakely & Horan 2008). A significant portion of these, totaling 56, are classified as HBLs. The localization uncertainty for extragalactic TeV sources is typically  $\gtrsim 10''$  (e.g., Archambault et al. 2013). To determine the infrared and X-ray properties of known TeV-emitting HBLs, we searched for their optical counterparts in the Simbad<sup>2</sup> database to obtain better localizations. Using these optical coordinates, all 56 TeV HBLs were found to have an infrared counterpart in the WISEA catalog within  $5''$ .

The first criterion we will use to identify TeV HBL candidates is based on their infrared colors. Massaro et al. (2011) showed that blazars occupy a strip in the *WISE* 3.4 – 4.6 – 12  $\mu$ m color-color diagram, making them distinguishable from other extragalactic sources. Massaro et al. (2012) demonstrated that gamma-ray emitting BL Lacs can further be separated from flat spectrum radio quasars based on their infrared colors. Using a similar approach as Massaro et al. (2013), we plot the infrared color-color diagram of the *WISE* counterparts of the 56 known TeV HBLs (Figure 1). We find that TeV HBLs cluster along the  $y = 0.84x - 1.05$  line

<sup>1</sup> <http://tevcats2.uchicago.edu>

<sup>2</sup> <https://simbad.cds.unistra.fr/simbad>

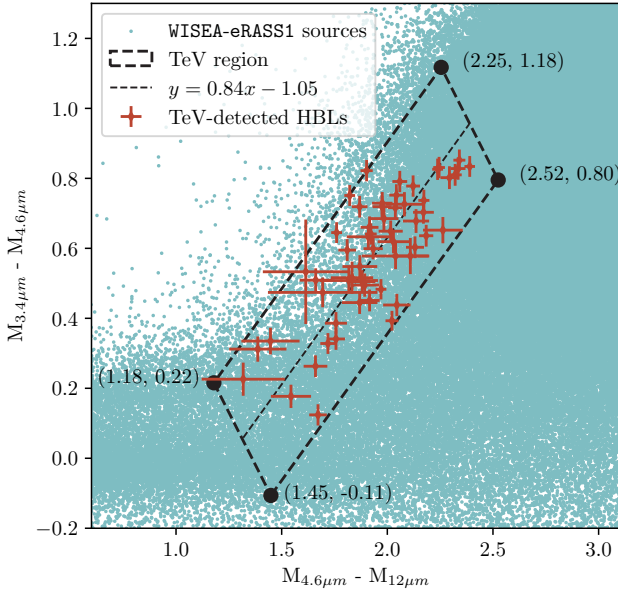


**Figure 1.** The *WISE* 3.4–4.6–12  $\mu\text{m}$  color-color plot for the 56 TBLs selected (red crosses). The dashed line corresponds to the regression line described 2. The black dashed rectangle corresponds to the maximum allowed separation (0.21) of the known TeV HBLs from this line. The turquoise points correspond to all WISEA sources found within the *eROSITA* footprint.

in the *WISE* 3.4–4.6–12  $\mu\text{m}$  color-color diagram. The farthest object from the best-fit line is at a distance of 0.21. In our search, we will require that new TeV HBL candidates be within a distance of less than 0.21 from the best-fit line determined from known TeV HBLs. The rectangle with boundaries shown in Figure 1 defines the region where TeV HBLs are found.

The next criterion for selecting TeV HBL candidates involves assessing their effective spectral index (or spectral slope) between the infrared and X-ray frequencies. First, we use the *WISE* coordinates of known TeV HBLs to find their X-ray counterparts in the *eROSITA* eRASS1 catalog. We match infrared sources with their closest X-ray counterpart as long as the separation is less than  $5''$ , which is the average positional error in the eRASS1 catalog (Merloni et al. 2024). Only 21 of the 56 known TeV HBLs are located in the western galactic hemisphere covered in the public eRASS1 data. To distinguish between HBLs and LBLs, we define the infrared to X-ray effective spectral index:

$$\alpha_{\text{IR-X}} = \frac{\log(F_{3.4\mu\text{m}}/F_{0.2-2.3\text{keV}})}{\log(\nu_{3.4\mu\text{m}}/\nu_{1\text{keV}})} \quad (1)$$

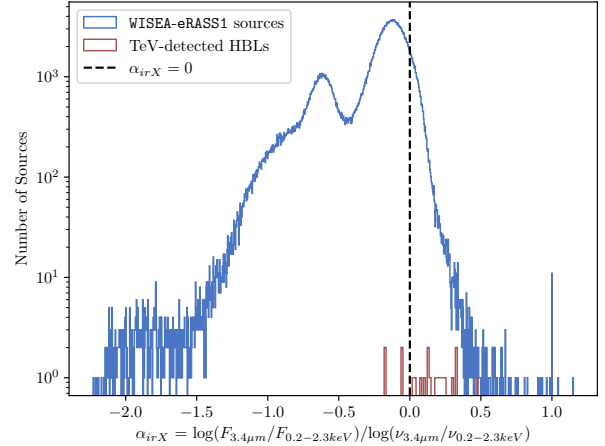


**Figure 2.** The distribution of  $\alpha_{\text{IR-X}}$  for all sources found in eRASS1 and WISEA (blue) and the 21 TBL sources found in the eRASS1 footprint (red). The dashed black line represents the our selection criterion of  $\alpha_{\text{IR-X}} > 0$ .

The distribution of  $\alpha_{\text{IR-X}}$  for all *WISE* sources with an *eROSITA* counterpart is shown in Figure 2. We require that new TeV HBL candidates have  $\alpha_{\text{IR-X}} \geq 0$ , as that cut maximizes the number of retained TeV HBLs while minimizing the number of potential candidates to be considered. We note that four known TeV HBLs in the eRASS1 footprint have  $\alpha_{\text{IR-X}} < 0$ : PKS 1440-389, 1ES 1215+303, TXS 1515-273, and PKS 0301-243. However, the  $\alpha_{\text{IR-X}}$  distribution for a general population of sources peaks at negative values, and relaxing the infrared to X-ray spectral index cut to include these four sources would significantly increase the number of seed infrared sources in our search and result in a higher potential for false positives. The observational properties of TeV-emitting HBLs are shown in Table A1.

### 3. SEARCH FOR NEW TEV HBL CANDIDATES

Based on the infrared and X-ray properties of known TeV-emitting HBLs, we define the following procedure to identify new candidate TeV HBLs (Figure 3). Our candidate list includes all sources that meet the following criteria:

- I. Infrared WISEA source detected with Vega magnitudes of less than 14.3, 13.8, and 12.2 at 3.4  $\mu\text{m}$ , 4.6  $\mu\text{m}$ , and 12  $\mu\text{m}$ , respectively;
- II. WISEA source has infrared colors similar to known gamma-ray blazars:  $1.25 \text{ mag} < M_{4.6\mu\text{m}} - M_{12\mu\text{m}} < 2.4 \text{ mag}$ ,  $0.05 \text{ mag} < M_{3.4\mu\text{m}} - M_{4.6\mu\text{m}} < 0.9 \text{ mag}$ ;
- III. WISEA source falls within a distance of 0.21 from the best-fit line in the infrared color-color diagram

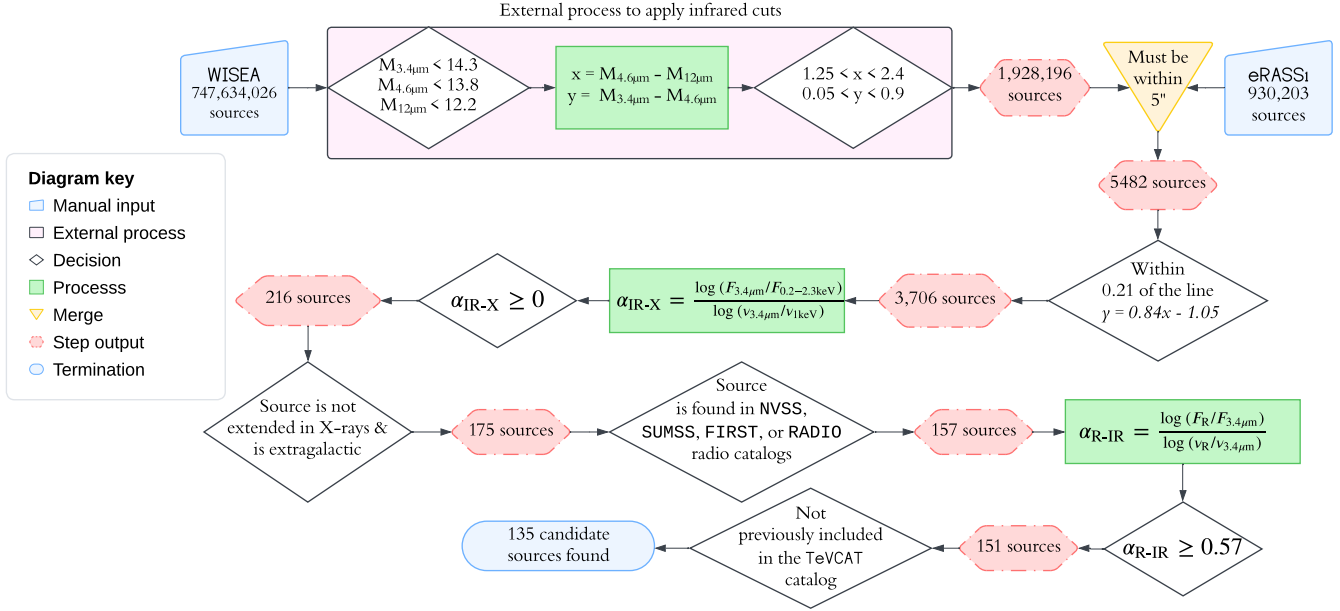


**Figure 3.** Description of the algorithm followed to identify TeV-emitting HBL candidates. The input surveys WISEA and eRASS1 are shown at the top in light blue. The resulting outcome of 135 objects is shown at the bottom, also in light blue. The number of objects that make it through each stage of filtering is shown in red boxes. Green boxes indicate parameters that are calculated based on catalog inputs.

where known TeV HBLs are located (Figure 1), as defined in Section 2;

- IV. Infrared WISEA source has an X-ray counterpart in the eRASS1 catalog within  $5''$ ;
- V. Source has an effective infrared to X-ray spectral index  $\alpha_{\text{IR-X}} \geq 0$  (Equation 1);
- VI. X-ray source is not listed as extended in eRASS1, guaranteeing that the X-ray object is compatible with a point source as expected for blazars;
- VII. Source has a galactic latitude  $|b| \geq 10^\circ$  to avoid the larger level source contamination expected near the galactic plane.
- VIII. Source has a counterpart in the NVSS, SUMSS, FIRST or RADIO radio catalogs.
- IX. The radio-to-infrared effective spectral index  $\alpha_{\text{R-IR}}$  of the source is larger than 0.57.

The criteria and procedures for identifying TeV-peaked BL Lac candidates are summarized in Figure 3. Criteria I-III focus on selecting sources with infrared characteristics similar to those of known TeV-emitting HBLs. All 56 known TeV-emitting HBLs have WISE magnitudes brighter than 14.3 mag, 13.8 mag, and 12.2 mag in the  $3.4\ \mu\text{m}$ ,  $4.6\ \mu\text{m}$ , and  $12\ \mu\text{m}$  bands, respectively (I). The slope of the jet-dominated synchrotron emission in the infrared band is effectively captured by infrared colors, with candidates required to have colors within these ranges (II):  $1.25 < M_{4.6\ \mu\text{m}} -$

$M_{12\ \mu\text{m}} < 2.4$  and  $0.05 < M_{3.4\ \mu\text{m}} - M_{4.6\ \mu\text{m}} < 0.9$ . The color-color criterion is refined by ensuring that candidate sources fall within 0.21 distance from the best-fit line in the infrared color-color diagram where the known TeV HBLs are located (III, Figure 1). The objects that pass these filters are all significantly detected by WISE with infrared colors resembling known TeV-emitting HBLs.

These candidates are then matched with their closest X-ray counterparts in the eRASS1 catalog (IV). We consider X-ray counterparts as long as the separation between the WISEA coordinates and the eROSITA X-ray counterpart is smaller than the average eRASS1 positional error of  $5''$ . Next, sources with  $\alpha_{\text{IR-X}} \geq 0$  are selected to identify objects peaking in the X-ray band (V). X-ray emission from blazars is unresolved at the  $18''$  spatial resolution characteristic of eROSITA. Thus, we reject objects with EXT parameter  $> 0$  (VI), denoting extended X-ray sources. Sources excluded by this criterion are listed in Table A2. Objects with galactic latitude  $|b| \leq 10^\circ$  are rejected to avoid source confusion (VII). The presence of a radio counterpart in the NVSS, FIRST, SUMSS, or other RADIO catalogs within  $5''$  of the WISE infrared source is also required (VIII). Objects that were excluded due to the lack of a known radio counterpart are listed in Table A3. The radio flux is used to calculate a radio-to-infrared spectral index:

$$\alpha_{\text{R-IR}} = \frac{\log(F_{\text{R}}/F_{3.4\ \mu\text{m}})}{\log(\nu_{\text{R}}/\nu_{3.4\ \mu\text{m}})} \quad (2)$$

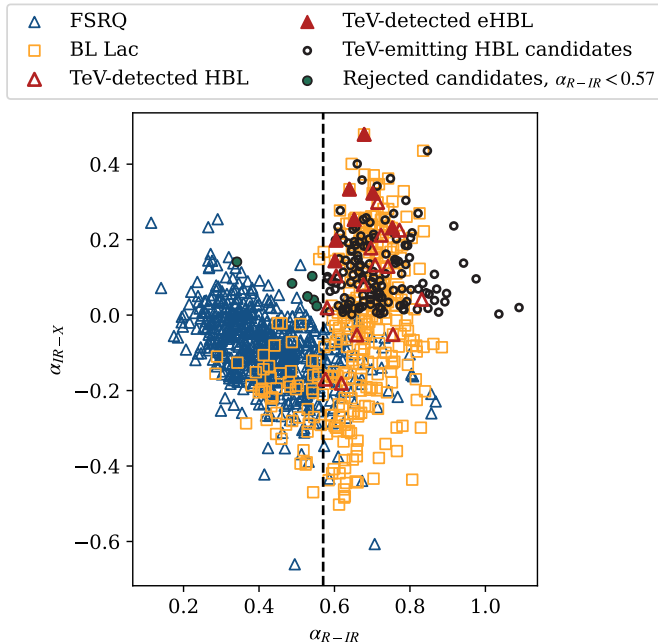


**Figure 4.** The ratio between the radio and IR fluxes, normalized by the ratios of their frequencies, plotted against  $\alpha_{\text{IR-X}}$  defined in Equation 1. BL Lac objects in ROMA-BZCAT are displayed as yellow triangles, while FSRQs are displayed as blue triangles. The 21 TeV-detected HBLs within the *eROSITA* footprint are shown as unfilled red triangles, while the ones designated as extreme HBLs (eHBLs) in TeVCat are shown as filled red triangles. The 135 candidate sources identified in our study are shown as open black circles. Sources that have passed all previous candidacy criteria but have  $\alpha_{\text{R-IR}} < 0.57$  are designated as green circles outlined in black.

where the radio flux is preferentially measured at  $\nu_{\text{R}} = 1.4$  GHz. As shown in Figure 4,  $\alpha_{\text{IR-X}}$  and  $\alpha_{\text{R-IR}}$  effectively characterize the synchrotron emission component of blazar candidates, distinguishing FSRQs with synchrotron peaks in the infrared band from BL Lacs with peaks at higher frequencies. TeV-emitting HBLs display harder effective spectral indices in both parameters, clustering in the top right quadrant of the plot. A final selection cut requires TeV-emitting candidates to have  $\alpha_{\text{R-IR}} \geq 0.57$  to exclude candidates whose synchrotron SED resembles those of FSRQs more than BL Lacs.

#### 4. A NEW LIST OF TEV HBL CANDIDATES

We have identified 135 TeV HBLs Candidates (THC) that meet the criteria outlined in Section 3. The properties of these candidates are listed in Table 1.

X-ray and TeV fluxes show a strong correlation in TeV-emitting HBLs (e.g., Katarzyński et al. 2005; Fos-

sati et al. 2008), with the 0.2-2.3 keV flux being a good predictor for TeV detectability (Figure 5, left). By using the measured X-ray flux as an indicator of expected TeV flux, we compile a list of the most promising candidates for observation with ground-based gamma-ray observatories. These promising candidates are categorized into objects on the northern (Table 2) and southern hemisphere (Table 3). Most of our candidates (76%) are located in the southern celestial hemisphere due to the larger overlap between this region and the western galactic hemisphere covered in the eRASS1 data release. In addition, the increased *eROSITA* exposure and subsequent increased source density around the southern ecliptic pole introduces a higher likelihood of our candidates being found on the southern hemisphere.

The probability of spurious spatial coincidences between an infrared-selected HBL-like object and an X-ray source in the eRASS1 catalog is negligible, leading to fewer than one expected spurious candidate in our sample. Using 100,000 random sky points placed within the eFEDS field (Brunner et al. 2022), which covers approximately  $\sim 140$  deg<sup>2</sup>, the random spatial correlation rate is 0.117%. Given that the eFEDS exposure is approximately 10 times that of the eRASS1 survey, we anticipate an even lower probability of random spatial association in the eRASS1 data set.

As part of our selection algorithm, we rejected objects with infrared properties similar to those of TeV-emitting HBLs that have an *eROSITA* counterpart that was labeled as an extended X-ray source. The 31 sources excluded from our list for this reason are listed in Table A2. These could still be objects of interest, as some of them could be associated with BL Lac-type blazars embedded in the core of a cluster of galaxies (similar to NGC 1275 and IC 310, located in the Perseus cluster), with the intracluster emission causing the X-ray counterpart to be extended in the *eROSITA* data. In addition, we discarded 18 sources because a radio counterpart could not be identified in the NVSS, FIRST, SUMSS, or other RADIO catalogs. These objects, listed in Table A3, could merit dedicated radio follow-up observations to determine whether a weak radio counterpart can be identified.

## 5. DISCUSSION AND CONCLUSIONS

Our search for TeV-emitting HBL candidates based on the *WISE* and *eROSITA* surveys has led to the identification of 135 promising objects. Among these 135 candidates, 49 (36%) are identified as BL Lacs in the ROMA-BZCAT catalog (Massaro et al. 2009, 2015), with an additional four categorized as BL Lac candidates. Our search finds a large overlap with the 3HSP

**Table 1.** List of TeV-emitting HBL candidates identified in our study, ordered by RA. The complete list of 135 objects can be accessed online in machine-readable format.

THC name	1eRASS	WISEA	RA	DEC	$F_{3.4\mu\text{m}}$ $\times 10^{-12}$ cgs	$F_{0.2-2.3\text{keV}}$ $\times 10^{-12}$ cgs	$F_{2-5\text{keV}}$ $\times 10^{-12}$ cgs	Radio Flux mJy	$\alpha_{\text{IR-IR}}$	$\alpha_{\text{IR-X}}$	4FGL	Massaro	3HSP
J0001-419	J000132.74-415525.2	J000132.7-415526	0.386	-41.924	0.70 $\pm$ 0.03	6.24 $\pm$ 0.25	1.89 $\pm$ 0.42	13.2	0.76	0.27	x	-	x
J0026-460	J002635.63-460109.9	J002635.5-460110	6.648	-46.019	0.68 $\pm$ 0.03	1.32 $\pm$ 0.11	0.00 $\pm$ 0.06	38.7	0.66	0.08	x	-	x
J0041-470	J004147.02-470136.9	J004146.9-470136	10.446	-47.027	1.02 $\pm$ 0.03	3.25 $\pm$ 0.17	1.65 $\pm$ 0.38	16.6	0.77	0.14	x	-	x
J0051-627	J005116.64-624204.3	J005116.4-624203	12.819	-62.701	1.50 $\pm$ 0.02	3.14 $\pm$ 0.14	0.99 $\pm$ 0.24	43.2	0.72	0.09	x	-	x
J0109-403	J010956.58-402050.9	J010956.4-402051	17.486	-40.347	0.76 $\pm$ 0.03	1.56 $\pm$ 0.11	0.36 $\pm$ 0.16	96.0	0.59	0.09	x	-	x
J0123-231	J012338.35-231058.7	J012338.1-231059	20.91	-23.183	0.65 $\pm$ 0.03	11.90 $\pm$ 0.30	4.83 $\pm$ 0.57	27.2	0.67	0.36	x	-	x
J0143-587	J014347.41-584551.4	J014347.6-584549	25.948	-58.764	1.16 $\pm$ 0.02	8.99 $\pm$ 0.24	2.14 $\pm$ 0.35	28.4	0.73	0.25	x	-	x
J0150-548	J015044.53-545005.0	J015044.4-545004	27.686	-54.835	0.62 $\pm$ 0.03	0.83 $\pm$ 0.08	0.13 $\pm$ 0.10	43.8	0.64	0.04	x	-	x
J0156-530	J015658.00-530200.0	J015657.9-530200	29.242	-53.033	0.76 $\pm$ 0.03	19.70 $\pm$ 0.38	10.00 $\pm$ 0.74	43.4	0.66	0.40	x	-	x
J0157-162	J015721.56-161420.9	J015721.4-161420	29.34	-16.239	0.93 $\pm$ 0.03	1.51 $\pm$ 0.10	0.49 $\pm$ 0.18	6.0	0.84	0.06	-	-	-
J0206-777	J020608.36-774343.7	J020608.1-774343	31.535	-77.729	1.01 $\pm$ 0.03	1.02 $\pm$ 0.07	0.11 $\pm$ 0.07	68.5	0.65	0.00	-	-	-
J0209-524	J020921.62-522922.8	J020921.6-522922	32.34	-52.49	2.26 $\pm$ 0.02	12.90 $\pm$ 0.29	3.45 $\pm$ 0.44	78.7	0.70	0.21	x	x	x
J0219-174	J021905.50-172513.0	J021905.5-172514	34.773	-17.42	1.06 $\pm$ 0.02	2.14 $\pm$ 0.12	0.92 $\pm$ 0.23	62.2	0.64	0.09	x	-	x
J0223-112	J022314.25-111738.4	J022314.3-111737	35.809	-11.294	0.66 $\pm$ 0.03	1.61 $\pm$ 0.10	0.35 $\pm$ 0.16	14.0	0.73	0.11	x	-	x
J0244-583	J024440.30-581954.5	J024440.2-581955	41.168	-58.332	1.48 $\pm$ 0.02	10.60 $\pm$ 0.22	3.88 $\pm$ 0.38	92.7	0.65	0.24	x	-	x
J0302-194	J030246.33-192425.3	J030246.3-192426	45.693	-19.407	0.76 $\pm$ 0.03	1.22 $\pm$ 0.08	0.63 $\pm$ 0.18	2.7	0.90	0.06	-	-	-
J0310-502	J031034.72-501631.1	J031034.8-501631	47.645	-50.275	0.85 $\pm$ 0.02	2.08 $\pm$ 0.09	0.63 $\pm$ 0.16	12.6	0.78	0.11	x	-	x
J0312-223	J031235.70-222117.2	J031235.7-222117	48.149	-22.355	0.55 $\pm$ 0.03	2.17 $\pm$ 0.10	0.13 $\pm$ 0.08	31.2	0.65	0.17	x	-	x
J0325-565	J032523.53-563544.6	J032523.2-563544	51.348	-56.596	3.90 $\pm$ 0.02	22.90 $\pm$ 0.54	9.67 $\pm$ 0.55	73.3	0.76	0.22	x	-	x
J0336-037	J033623.79-034738.6	J033623.8-034739	54.099	-3.794	1.06 $\pm$ 0.03	7.04 $\pm$ 0.20	4.57 $\pm$ 0.49	53.8	0.66	0.13	x	-	x
J0338-287	J033859.60-284619.9	J033859.4-284619	54.748	-28.772	0.88 $\pm$ 0.03	2.24 $\pm$ 0.10	0.86 $\pm$ 0.18	40.7	0.66	0.22	x	-	x
J0352-685	J035257.48-683117.0	J035257.5-683118	58.24	-68.521	3.96 $\pm$ 0.02	8.84 $\pm$ 0.19	3.28 $\pm$ 0.27	409.3	0.61	0.10	x	-	x
J0353-363	J035305.04-362308.4	J035304.9-362307	58.271	-36.386	0.61 $\pm$ 0.03	3.23 $\pm$ 0.11	0.69 $\pm$ 0.15	6.2	0.80	0.20	x	-	x
J0355-187	J035513.28-184308.5	J035513.3-184308	58.805	-18.719	0.55 $\pm$ 0.03	1.38 $\pm$ 0.09	0.34 $\pm$ 0.14	39.9	0.62	0.11	x	-	x
J0356-393	J035618.88-392141.2	J035618.9-392141	59.079	-39.361	0.66 $\pm$ 0.03	3.40 $\pm$ 0.11	1.43 $\pm$ 0.21	22.6	0.69	0.20	-	-	-
J0427-185	J042733.35-183010.3	J042733.3-183010	66.889	-18.503	0.87 $\pm$ 0.03	1.48 $\pm$ 0.10	0.32 $\pm$ 0.15	14.5	0.76	0.07	x	-	x
J0443-418	J044328.41-415156.0	J044328.3-415156	70.868	-41.866	0.55 $\pm$ 0.03	1.17 $\pm$ 0.07	0.23 $\pm$ 0.10	26.8	0.67	0.09	x	-	x
J0448-165	J044837.61-163243.2	J044837.6-163242	72.157	-16.545	0.74 $\pm$ 0.03	4.28 $\pm$ 0.17	2.25 $\pm$ 0.38	58.7	0.62	0.22	x	-	x
J0452-000	J045249.50-000152.0	J045249.3-000153	73.206	-0.031	0.65 $\pm$ 0.03	0.79 $\pm$ 0.08	0.63 $\pm$ 0.21	27.2	0.67	0.02	-	-	-
J0458+089	J045834.80+085643.4	J045834.7+085644	74.645	8.945	0.60 $\pm$ 0.03	0.93 $\pm$ 0.09	0.37 $\pm$ 0.18	19.5	0.70	0.05	-	-	-
J0504-099	J050419.51-095632.9	J050419.4-095632	76.081	-9.942	0.56 $\pm$ 0.03	1.41 $\pm$ 0.10	0.57 $\pm$ 0.20	25.8	0.66	0.11	x	-	x
J0506-545	J050657.81-543503.7	J050657.6-543503	76.741	-54.584	1.16 $\pm$ 0.08	1.42 $\pm$ 0.06	0.23 $\pm$ 0.07	18.0	0.77	0.02	x	-	x
J0509-040	J050938.18-040045.8	J050938.1-040046	77.409	-4.013	0.77 $\pm$ 0.03	3.86 $\pm$ 0.17	2.17 $\pm$ 0.39	70.5	0.60	0.20	x	-	x
J0536-337	J053629.06-334302.5	J053629.1-334303	84.121	-33.717	1.76 $\pm$ 0.02	2.04 $\pm$ 0.10	0.60 $\pm$ 0.17	94.3	0.65	0.02	x	x	x
J0543-555	J054357.22-553207.3	J054357.0-553204	85.988	-55.535	2.09 $\pm$ 0.02	39.80 $\pm$ 0.74	14.60 $\pm$ 0.47	43.4	0.75	0.36	x	x	x

Col. (1) THC Designation

Cols. (2-3) *eROSITA* and *WISE* names

Cols. (4-5) Right ascension and declination of the *WISE* counterpart.

Col. (6) *WISE* flux in the 3.4 $\mu\text{m}$  band

Col. (7) *eRASS1* flux in the 0.2 - 2.3 keV band

Col. (8) *eRASS1* flux in the 2 - 5 keV band

Col. (9) The radio flux from *SUMSS*, *WISS*, or *FIRST*. If the source is found in all 3 catalogs, the *WISS* flux is listed, if the source is found in only *SUMSS* and *FIRST*, the *FIRST* flux is listed. If the source is from *SUMSS*, it is the flux at 843 MHz; otherwise, it is the flux at 1.4 GHz.

Cols. (10-11) Radio to infrared, and infrared to X-ray effective spectral index.

Cols. (12-14) A check of whether or not the source appears in the 4FGL (Abdollahi et al. 2020), Massaro (Massaro et al. 2013), and 3HSP (Chang et al. 2019) catalogs.

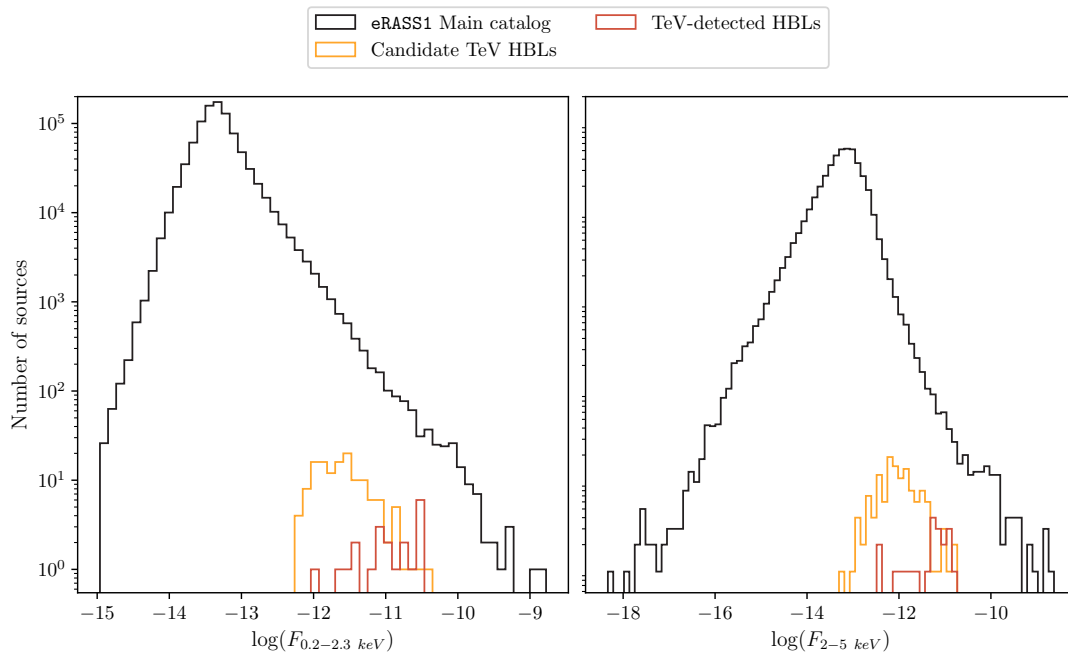


**Figure 5.** Distribution of X-ray fluxes for the TeV candidate blazars in different bands from the eRASS1 catalog, compared to the fluxes of all sources in the eROSITA survey.

**Table 2.** Most promising TeV-peaked HBL candidates with northern declination, ranked by their 0.2-2.3 keV flux. The last column lists sources also selected in Costamante (2020).

Name	$F_{3.4\mu\text{m}}$ $\times 10^{-12}$ cgs	$F_{0.2-2.3\text{keV}}$ $\times 10^{-12}$ cgs	$\alpha_{\text{IR-X}}$	C20
J1404+040	$1.02 \pm 0.03$	$4.52 \pm 0.17$	0.18	-
J0909+311	$1.32 \pm 0.03$	$4.42 \pm 0.23$	0.15	-
J0837+149	$1.70 \pm 0.02$	$3.51 \pm 0.21$	0.09	x
J1140+154	$1.18 \pm 0.03$	$3.41 \pm 0.21$	0.13	x
J1138+033	$1.07 \pm 0.03$	$3.27 \pm 0.19$	0.14	-
J1107+150	$0.76 \pm 0.03$	$3.11 \pm 0.20$	0.17	-
J0747+090	$0.83 \pm 0.03$	$2.98 \pm 0.20$	0.14	-
J1149+246	$0.61 \pm 0.03$	$2.95 \pm 0.19$	0.19	-
J0723+208	$0.82 \pm 0.03$	$2.64 \pm 0.19$	0.14	-
J0723+208	$1.03 \pm 0.02$	$1.17 \pm 0.09$	0.02	x

**Table 3.** Most promising TeV-peaked HBL candidates with southern declination, ranked by their 0.2-2.3 keV flux. The last column lists sources also selected in Costamante (2020).

Name	$F_{3.4\mu\text{m}}$ $\times 10^{-12}$ cgs	$F_{0.2-2.3\text{keV}}$ $\times 10^{-12}$ cgs	$\alpha_{\text{IR-X}}$	C20
J0543-555	$2.09 \pm 0.02$	$39.8 \pm 0.7$	0.36	-
J1503-156	$0.86 \pm 0.03$	$29.6 \pm 0.7$	0.44	-
J0325-565	$3.90 \pm 0.02$	$22.9 \pm 0.5$	0.22	-
J0156-530	$0.76 \pm 0.03$	$19.7 \pm 0.4$	0.40	-
J1409-452	$2.68 \pm 0.02$	$15.8 \pm 0.3$	0.22	-
J1440-387	$0.86 \pm 0.03$	$13.8 \pm 0.3$	0.34	-
J1548-228	$2.86 \pm 0.02$	$13.0 \pm 0.3$	0.19	-
J0209-524	$2.26 \pm 0.02$	$12.9 \pm 0.3$	0.21	-
J0558-386	$1.31 \pm 0.02$	$12.5 \pm 0.2$	0.28	-
J0123-231	$0.65 \pm 0.03$	$11.9 \pm 0.3$	0.36	-
J0244-583	$2.26 \pm 0.02$	$10.6 \pm 0.2$	0.24	x
J0509-040	$0.77 \pm 0.02$	$3.9 \pm 0.2$	0.20	x
J0506-543	$1.16 \pm 0.09$	$1.4 \pm 0.1$	0.02	x

catalog (Chang et al. 2019), which identified 2013 HBL blazar candidates based on radio-to-X-ray effective spectral indices and a radio flux cut. Specifically, 112 of the 135 candidates (83%) are also featured in the 3HSP catalog. The 3HSP catalog selects 2013 sources with  $\nu_{\text{peak}} \gtrsim 4$  eV without specifically selecting for TeV emitters, and goes an order of magnitude deeper in X-ray flux ( $4 \times 10^{-14}$  erg cm $^{-2}$  s $^{-1}$ ) than the weakest X-ray flux in our final candidate list ( $6 \times 10^{-13}$  erg cm $^{-2}$  s $^{-1}$ ). Half of our candidates not present in the 3HSP catalog were not detected by *ROSAT*. A smaller overlap is found with the TeV candidates identified in Massaro et al. (2013), with 13 sources from their candidate list also found in our

study. We observed that a number of sources had their infrared fluxes revised between the *WISE* data release in 2012 used in Massaro et al. (2013) and the 2024 WISEA data release, resulting in some of the sources no longer making the infrared flux and color cuts. Our selection criterion based on the infrared to X-ray spectra slope is also more stringent than the infrared to X-ray flux ratio cut in Massaro et al. (2013).

A recent, dedicated search for TeV-peaked BL Lac candidates with a gamma-ray peak  $> 1$  TeV utilizes X-ray flux and the effective spectral index between the X-ray and gamma-ray bands to identify 47 candidates (Costamante 2020). This search is particularly effective in finding candidates with low radio flux. Among the 16 sources identified by Costamante (2020) located in the western galactic hemisphere, 6 are also found in our search. On the other hand, our algorithm did not select 10 sources listed in Costamante (2020): six fail the  $M_{3.4\mu\text{m}}$  threshold, and three do not fit within the infrared color-color selection criteria. The remaining source narrowly misses our  $\alpha_{\text{IR-X}}$  cut. The candidates with lower radio flux in Costamante (2020) are likely to exhibit lower infrared flux as well, making our searches complementary. All sources identified both in our search and by Costamante (2020) are listed in Tables 2 and 3, and should be considered prime TeV-emitting eHBL candidates.

We note that 20 of our candidates (15%) are not listed in the 3HSP catalog, the ROMA-BZCAT catalog, or the Fermi Large Area Telescope Fourth Source Catalog (4FGL; Abdollahi et al. 2020), and 26 candidates (19%) do not have a *ROSAT* counterpart (2RXS catalog, Boller et al. 2016) showing the power of the depth of the eRASS1 survey to reveal new TeV HBL candidates that may have eluded detection in previous searches.

A second notable advantage of *eROSITA* over *ROSAT* is its extended energy range, covering higher X-ray energies. *eROSITA* is sensitive in the 0.2–8 keV band, whereas *ROSAT* was limited to the 0.1–2.4 keV range. The initial data release from *eROSITA* includes two catalogs: a main catalog of sources detected between 0.2 and 2.3 keV, and a hard source catalog for sources detected between 2.3 and 5 keV (Merloni et al. 2024). While all 21 TeV-detected HBLs in the western galactic hemisphere were significantly detected in the main eRASS1 catalog, two were not found in the *eROSITA* hard catalog. Figure 6 illustrates that some TeV HBLs appear at hard X-ray fluxes below the threshold at which the eRASS1 hard catalog can be considered complete. Conversely, the eRASS1 main source catalog appears to be complete down to the flux levels of the weakest TeV-detected HBLs. For this reason, we used the main

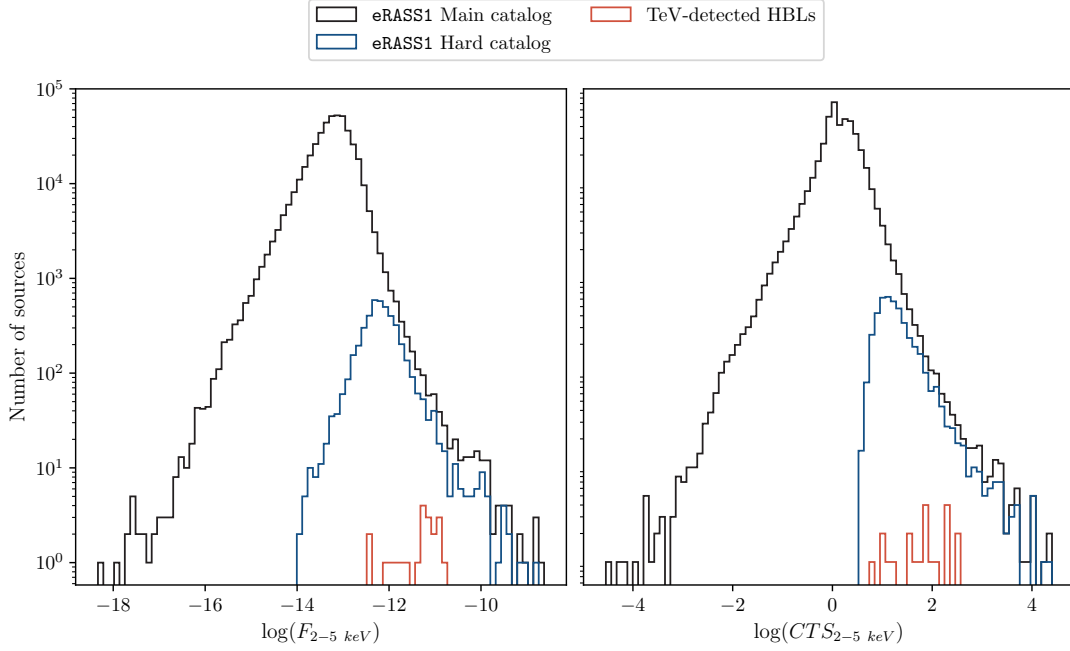


**Figure 6.** The flux and counts distribution in the 2.0-5.0 keV band for the main eRASS1 catalog (black) and hard eRASS1 catalog (blue) compared with the flux and counts for TeV-detected HBLs (red).

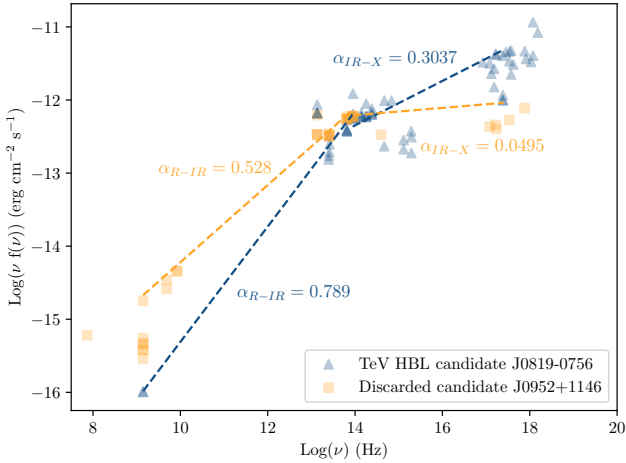


**Figure 7.** Example of the synchrotron SED of one of our selected candidates (blue triangles) compared to a potential candidate that is discarded by the  $\alpha_{\text{IR-IR}}$  cut (yellow squares). Quasar-like sources can make it through our selection criteria based on infrared flux and spectrum and display an  $\alpha_{\text{IR-X}}$  similar to that of TeV HBLs even though their synchrotron peak is probably in the infrared band and their X-ray flux, showing a hard very hard spectrum, samples the rising edge of their high-energy spectral component. These quasar-like objects will tend to display larger jet powers than BL Lacs, and their excess radio flux can be used to discriminate them from BL Lacs using the  $\alpha_{\text{R-IR}}$  criterion (See Section 3).

eRASS1 catalog, rather than the hard catalog, to characterize the X-ray emission of our source candidates.

In our study, we have introduced the radio-IR-X spectral slopes to separate flat spectrum radio quasars from BL Lacs (Figure 4). As seen in Figure 7, quasar-like sources can meet our selection criteria that rely on infrared flux and spectral features, and display an  $\alpha_{\text{IR-X}}$  similar to that found in TeV HBLs. This happens even though their synchrotron peak is likely in the infrared range, while their X-ray flux, with a particularly hard spectrum, samples the rising phase of their high-energy spectral emission. These quasar-like sources typically have more powerful jets compared to BL Lacs, and their additional radio flux distinguishes them from BL Lacs using the  $\alpha_{\text{R-IR}}$  criterion. In addition, extreme HBLs with a high-energy spectral component peaking beyond 1 TeV do appear to have higher  $\alpha_{\text{IR-X}}$  values than regular TeV-detected HBLs (Figure 4), yielding yet another metric that can be used to select extreme objects.

HBLs are brightest in the X-ray band due to the location of their synchrotron peak. Our study takes advantage of the recently released eRASS1 catalog, which currently constitutes the deepest survey where HBLs can be found. The *Fermi*-LAT allsky survey in the gamma-ray band is similarly deep. However, with LAT sensitivity peaking at a few GeV, high LAT fluxes select sources with soft GeV spectra rather than the hard GeV spectra expected for HBLs. As noted by Costamante (2020), the most extreme blazars might not appear in radio loud AGN catalogs due to their low jet power and consequently weak radio emission compared to the bright

optical flux from the host galaxy, reducing their radio loudness parameter. Current and future image atmospheric Cherenkov telescopes continue to be the most efficient means to find and characterize TeV-emitting BL Lacs. On the other hand, gamma-ray observatories based on particle-sampling arrays have the advantage of a large field of view and efficient duty cycle, carrying out effective surveys of the TeV sky. However, their limited sensitivity below 1 TeV reduces their effectiveness for objects with redshifts  $z \gtrsim 0.1$  due to the absorption of TeV gamma rays by the extragalactic background light. LHAASO has detected gamma-ray emission from four blazars (Cao et al. 2024), while HAWC has significant detections of Mrk 241 and Mrk 501, along with

evidence for emission from three other blazars (Albert et al. 2021). The results of our study, listed in Table 1, offer promising candidates for pointed searches for new TeV-emitting blazars, which can be conducted by HESS, VERITAS, MAGIC and LST-1, as well as by CTAO once it begins its operations.

*Facilities:* *eROSITA*, WISE.

*Software:* *astropy* (Astropy Collaboration et al. 2013, 2018, 2022), *HEASoft* (Heasarc 2014)

CM and AG acknowledge financial support from the McDonnell Center for the Space Sciences at Washington University in Saint Louis that made this study possible.

## REFERENCES

- Abdollahi, S., Acero, F., Ackermann, M., et al. 2020, *The Astrophysical Journal Supplement Series*, 247, 33, doi: [10.3847/1538-4365/ab6bcb](https://doi.org/10.3847/1538-4365/ab6bcb)
- Acciari, V. A., Agudo, I., Aniello, T., et al. 2023, *A&A*, 670, A145, doi: [10.1051/0004-6361/202244126](https://doi.org/10.1051/0004-6361/202244126)
- Aharonian, F., Buckley, J., Kifune, T., & Sinnis, G. 2008, *Reports on Progress in Physics*, 71, 096901, doi: [10.1088/0034-4885/71/9/096901](https://doi.org/10.1088/0034-4885/71/9/096901)
- Aharonian, F., Akhperjanian, A. G., Bazer-Bachi, A. R., et al. 2006, *Nature*, 440, 1018, doi: [10.1038/nature04680](https://doi.org/10.1038/nature04680)
- Aharonian, F., Aschersleben, J., Backes, M., et al. 2023, *ApJL*, 950, L16, doi: [10.3847/2041-8213/acd777](https://doi.org/10.3847/2041-8213/acd777)
- Albert, A., Alvarez, C., Angeles Camacho, J. R., et al. 2021, *ApJ*, 907, 67, doi: [10.3847/1538-4357/abca9a](https://doi.org/10.3847/1538-4357/abca9a)
- Archambault, S., Arlen, T., Aune, T., et al. 2013, *ApJ*, 776, 69, doi: [10.1088/0004-637X/776/2/69](https://doi.org/10.1088/0004-637X/776/2/69)
- Archambault, S., Archer, A., Benbow, W., et al. 2017, *ApJ*, 835, 288, doi: [10.3847/1538-4357/835/2/288](https://doi.org/10.3847/1538-4357/835/2/288)
- Astropy Collaboration, Robitaille, T. P., Tollerud, E. J., et al. 2013, *A&A*, 558, A33, doi: [10.1051/0004-6361/201322068](https://doi.org/10.1051/0004-6361/201322068)
- Astropy Collaboration, Price-Whelan, A. M., Sipőcz, B. M., et al. 2018, *AJ*, 156, 123, doi: [10.3847/1538-3881/aabc4f](https://doi.org/10.3847/1538-3881/aabc4f)
- Astropy Collaboration, Price-Whelan, A. M., Lim, P. L., et al. 2022, *ApJ*, 935, 167, doi: [10.3847/1538-4357/ac7c74](https://doi.org/10.3847/1538-4357/ac7c74)
- Biteau, J., & Williams, D. A. 2015, *ApJ*, 812, 60, doi: [10.1088/0004-637X/812/1/60](https://doi.org/10.1088/0004-637X/812/1/60)
- Biteau, J., Prandini, E., Costamante, L., et al. 2020, *Nature Astronomy*, 4, 124, doi: [10.1038/s41550-019-0988-4](https://doi.org/10.1038/s41550-019-0988-4)
- Blandford, R., Meier, D., & Readhead, A. 2019, *Annual Review of Astronomy and Astrophysics*, 57
- Boller, T., Freyberg, M. J., Trümper, J., et al. 2016, *A&A*, 588, A103, doi: [10.1051/0004-6361/201525648](https://doi.org/10.1051/0004-6361/201525648)
- Bonnoli, G., Tavecchio, F., Ghisellini, G., & Sbarrato, T. 2015, *MNRAS*, 451, 611, doi: [10.1093/mnras/stv953](https://doi.org/10.1093/mnras/stv953)
- Brunner, H., Liu, T., Lamer, G., et al. 2022, *A&A*, 661, A1, doi: [10.1051/0004-6361/202141266](https://doi.org/10.1051/0004-6361/202141266)
- Cao, Z., Aharonian, F., An, Q., et al. 2024, *ApJS*, 271, 25, doi: [10.3847/1538-4365/acfd29](https://doi.org/10.3847/1538-4365/acfd29)
- Chang, Y.-L., Arsioli, B., Giommi, P., Padovani, P., & Brandt, C. H. 2019, *Astronomy & Astrophysics*, 632, A77, doi: [10.1051/0004-6361/201834526](https://doi.org/10.1051/0004-6361/201834526)
- Chen, W., Buckley, J. H., & Ferrer, F. 2015, *PhRvL*, 115, 211103, doi: [10.1103/PhysRevLett.115.211103](https://doi.org/10.1103/PhysRevLett.115.211103)
- Costamante, L. 2020, *MNRAS*, 491, 2771, doi: [10.1093/mnras/stz3018](https://doi.org/10.1093/mnras/stz3018)
- Costamante, L., Bonnoli, G., Tavecchio, F., et al. 2018, *MNRAS*, 477, 4257, doi: [10.1093/mnras/sty857](https://doi.org/10.1093/mnras/sty857)
- Costamante, L., & Ghisellini, G. 2002, *A&A*, 384, 56, doi: [10.1051/0004-6361:20011749](https://doi.org/10.1051/0004-6361:20011749)
- Costamante, L., Ghisellini, G., Giommi, P., et al. 2001, *A&A*, 371, 512, doi: [10.1051/0004-6361:20010412](https://doi.org/10.1051/0004-6361:20010412)
- Errando, M., & Saito, T. 2023, in *Handbook of X-ray and Gamma-ray Astrophysics*, 144, doi: [10.1007/978-981-16-4544-0\\_61-1](https://doi.org/10.1007/978-981-16-4544-0_61-1)
- Finke, J. D., Reyes, L. C., Georganopoulos, M., et al. 2015, *ApJ*, 814, 20, doi: [10.1088/0004-637X/814/1/20](https://doi.org/10.1088/0004-637X/814/1/20)
- Fossati, G., Buckley, J. H., Bond, I. H., et al. 2008, *ApJ*, 677, 906, doi: [10.1086/527311](https://doi.org/10.1086/527311)
- Giommi, P., Piranomonte, S., Perri, M., & Padovani, P. 2005, *A&A*, 434, 385, doi: [10.1051/0004-6361:20041789](https://doi.org/10.1051/0004-6361:20041789)
- H. E. S. S. Collaboration, Abramowski, A., Acero, F., et al. 2011, *A&A*, 529, A49, doi: [10.1051/0004-6361/201116545](https://doi.org/10.1051/0004-6361/201116545)

- Healey, S. E., Romani, R. W., Cotter, G., et al. 2008, *ApJS*, 175, 97, doi: [10.1086/523302](https://doi.org/10.1086/523302)
- Heasarc. 2014, HEASoft: Unified Release of FTOOLS and XANADU, Astrophysics Source Code Library, record ascl:1408.004. <http://ascl.net/1408.004>
- Ivezić, Ž., Menou, K., Knapp, G. R., et al. 2002, *AJ*, 124, 2364, doi: [10.1086/344069](https://doi.org/10.1086/344069)
- Kara, E., Errando, M., Max-Moerbeck, W., et al. 2012, *ApJ*, 746, 159, doi: [10.1088/0004-637X/746/2/159](https://doi.org/10.1088/0004-637X/746/2/159)
- Katarzyński, K., Ghisellini, G., Tavecchio, F., et al. 2005, *A&A*, 433, 479, doi: [10.1051/0004-6361:20041556](https://doi.org/10.1051/0004-6361:20041556)
- Kellermann, K. I., Sramek, R., Schmidt, M., Shaffer, D. B., & Green, R. 1989, *AJ*, 98, 1195, doi: [10.1086/115207](https://doi.org/10.1086/115207)
- Mainzer, A., Bauer, J., Grav, T., et al. 2011, *ApJ*, 731, 53, doi: [10.1088/0004-637X/731/1/53](https://doi.org/10.1088/0004-637X/731/1/53)
- Marcotulli, L., Di Mauro, M., & Ajello, M. 2020, *ApJ*, 896, 6, doi: [10.3847/1538-4357/ab8cbd](https://doi.org/10.3847/1538-4357/ab8cbd)
- Massaro, E., Giommi, P., Leto, C., et al. 2009, *A&A*, 495, 691, doi: [10.1051/0004-6361:200810161](https://doi.org/10.1051/0004-6361:200810161)
- Massaro, E., Maselli, A., Leto, C., et al. 2015, *Ap&SS*, 357, 75, doi: [10.1007/s10509-015-2254-2](https://doi.org/10.1007/s10509-015-2254-2)
- Massaro, F., D’Abrusco, R., Ajello, M., Grindlay, J. E., & Smith, H. A. 2011, *ApJL*, 740, L48, doi: [10.1088/2041-8205/740/2/L48](https://doi.org/10.1088/2041-8205/740/2/L48)
- Massaro, F., D’Abrusco, R., Tosti, G., et al. 2012, *The Astrophysical Journal*, 750, 138, doi: [10.1088/0004-637x/750/2/138](https://doi.org/10.1088/0004-637x/750/2/138)
- Massaro, F., Paggi, A., Errando, M., et al. 2013, *The Astrophysical Journal Supplement Series*, 207, 16, doi: [10.1088/0067-0049/207/1/16](https://doi.org/10.1088/0067-0049/207/1/16)
- Mazin, D., & Raue, M. 2007, *A&A*, 471, 439, doi: [10.1051/0004-6361:20077158](https://doi.org/10.1051/0004-6361:20077158)
- Merloni, A., Lamer, G., Liu, T., et al. 2024, *Astronomy & Astrophysics*, 682, A34, doi: [10.1051/0004-6361/202347165](https://doi.org/10.1051/0004-6361/202347165)
- Mukherjee, R., Gotthelf, E. V., Halpern, J., & Tavani, M. 2000, *ApJ*, 542, 740, doi: [10.1086/317054](https://doi.org/10.1086/317054)
- Neronov, A., & Vovk, I. 2010, *Science*, 328, 73, doi: [10.1126/science.1184192](https://doi.org/10.1126/science.1184192)
- Padovani, P., & Giommi, P. 1995, *ApJ*, 444, 567, doi: [10.1086/175631](https://doi.org/10.1086/175631)
- Sitarek, J. 2022, *Galaxies*, 10, 21, doi: [10.3390/galaxies10010021](https://doi.org/10.3390/galaxies10010021)
- Urry, C. M., & Padovani, P. 1995, *PASP*, 107, 803, doi: [10.1086/133630](https://doi.org/10.1086/133630)
- Vandenbroucke, J., Buehler, R., Ajello, M., et al. 2010, *ApJL*, 718, L166, doi: [10.1088/2041-8205/718/2/L166](https://doi.org/10.1088/2041-8205/718/2/L166)
- Wakely, S. P., & Horan, D. 2008, in *International Cosmic Ray Conference*, Vol. 3, International Cosmic Ray Conference, 1341–1344
- Wright, E. L., Eisenhardt, P. R. M., Mainzer, A. K., et al. 2010, *The Astronomical Journal*, 140, 1868, doi: [10.1088/0004-6256/140/6/1868](https://doi.org/10.1088/0004-6256/140/6/1868)

## APPENDIX

In this Appendix, we include three tables as supplementary information. Table [A1](#) lists the properties of TeV-detected HBLs. Table [A2](#) lists infrared sources of interest that were spatially associated with an extended X-ray counterpart in the *eROSITA* survey. Table [A3](#) lists infrared sources of interest with an *eROSITA* counterpart for which we could not find a radio counterpart in the NVSS, FIRST, SUMSS, or other RADIO catalogs.

**Table A1.** Radio, infrared and X-ray properties of TeV-detected HBLs, ordered by RA.

Name	$F_{3.4\mu\text{m}}$	$F_{0.2-2.3\text{keV}}$	$F_{2-5\text{keV}}$	Radio Flux	$\alpha_{\text{R-IR}}$	$\alpha_{\text{IR-X}}$
	$\times 10^{-12}$ cgs	$\times 10^{-12}$ cgs	$\times 10^{-12}$ cgs	mJy		
SHBL J001355.9-185406	2.69 ± 0.08	–	–	29.2	0.80	–
KUV 00311-1938	3.33 ± 0.07	–	–	18.5	0.86	–
1ES 0033+595	4.27 ± 0.09	–	–	147.3	0.69	–
RGB J0136+391	5.01 ± 0.11	–	–	60.0	0.79	–
RGB J0152+017	4.88 ± 0.10	–	–	61.4	0.78	–
TXS 0210+515	6.64 ± 0.14	–	–	294.3	0.67	–
1ES 0229+200	2.27 ± 0.06	–	–	82.4	0.69	–
1RXS J023832.6-311658	2.66 ± 0.05	30.3 ± 1.1	12.53 ± 0.75	71.0	0.71	0.30
PKS 0301-243	9.10 ± 0.18	2.09 ± 0.10	0.38 ± 0.13	700.2	0.62	–0.18
RBS 0413	1.18 ± 0.03	–	–	20.9	0.75	–
1ES 0347-121	0.61 ± 0.02	29.8 ± 0.7	15.3 ± 0.9	23.9	0.68	0.48
1ES 0414+009	2.26 ± 0.05	17.8 ± 0.5	13.49 ± 2.02	119.6	0.65	0.25
PKS 0447-439	16.9 ± 0.3	32.6 ± 0.4	6.2 ± 0.5	382.1	0.68	0.08
1ES 0502+675	2.21 ± 0.05	–	–	25.4	0.79	–
PKS 0548-322	3.82 ± 0.08	19.2 ± 0.4	8.5 ± 0.7	343.7	0.60	0.20
RX J0648.7+1516	2.24 ± 0.05	6.61 ± 0.29	4.4 ± 0.7	64.2	0.71	0.13
1ES 0647+250	3.99 ± 0.08	22.3 ± 0.5	10.00 ± 1.08	96.2	0.72	0.21
RGB J0710+591	2.48 ± 0.05	–	–	63.0	0.72	–
PGC 2402248	3.67 ± 0.08	–	–	23.5	0.84	–
1ES 0806+524	6.44 ± 0.13	–	–	182.4	0.71	–
1RXS J081201.8+023735	1.36 ± 0.03	3.18 ± 0.20	0.89 ± 0.31	122.1	0.60	0.10
RBS 0723	1.07 ± 0.02	14.8 ± 0.4	6.8 ± 0.9	32.8	0.70	0.32
MRC 0910-208	3.53 ± 0.07	11.4 ± 0.3	5.9 ± 0.7	328.4	0.60	0.14
1RXS J101015.9-311909	2.27 ± 0.05	9.6 ± 0.3	5.1 ± 0.7	73.5	0.70	0.18
1ES 1011+496	7.01 ± 0.15	–	–	377.7	0.65	–
1ES 1101-232	1.98 ± 0.04	29.9 ± 0.6	12.9 ± 1.0	120.3	0.64	0.33
Markarian 421	47.4 ± 1.0	–	–	767.4	0.76	–
Markarian 180	9.75 ± 0.19	–	–	327.1	0.69	–
RX J1136.5+6737	1.82 ± 0.04	–	–	45.3	0.72	–
1ES 1215+303	11.72 ± 0.24	7.6 ± 0.3	1.3 ± 0.4	571.6	0.66	–0.05
1ES 1218+304	4.11 ± 0.08	27.0 ± 0.6	6.8 ± 0.8	71.0	0.75	0.23
MS 1221.8+2452	1.25 ± 0.03	3.56 ± 0.18	1.2 ± 0.3	24.5	0.74	0.13
1ES 1312-423	1.49 ± 0.03	9.29 ± 0.22	5.3 ± 0.5	13.9	0.77	0.23
RBS 1366	1.37 ± 0.05	–	–	39.5	0.71	–
PKS 1424+240	25.1 ± 0.5	–	–	429.7	0.75	–
H 1426+428	2.26 ± 0.05	–	–	58.0	0.72	–
1ES 1440+122	1.78 ± 0.06	–	–	68.8	0.68	–
PKS 1440-389	6.46 ± 0.14	4.26 ± 0.15	1.65 ± 0.28	109.8	0.76	–0.05
TXS 1515-273	4.60 ± 0.10	1.16 ± 0.10	0.40 ± 0.18	564.2	0.58	–0.17
PG 1553+113	19.4 ± 0.4	–	–	312.0	0.76	–
Markarian 501	32.4 ± 0.7	–	–	1558.0	0.66	–
H 1722+119	6.19 ± 0.13	–	–	120.4	0.74	–
1ES 1727+502	4.32 ± 0.09	–	–	200.7	0.66	–
1ES 1741+196	6.10 ± 0.13	–	–	301.2	0.66	–
HESS J1943+213	1.65 ± 0.18	–	–	102.6	0.64	–
1RXS J195815.6-301119	2.55 ± 0.05	–	–	127.5	0.66	–
1ES 1959+650	12.98 ± 0.27	–	–	249.6	0.74	–
PKS 2005-489	23.6 ± 0.5	27.6 ± 0.6	6.4 ± 0.8	1299.0	0.58	0.02
1ES 2037+521	5.44 ± 0.11	–	–	40.7	0.83	–
PKS 2155-304	57.8 ± 1.2	–	–	489.3	0.82	–
RGB J2243+203	4.71 ± 0.10	–	–	108.5	0.73	–
B3 2247+381	4.18 ± 0.09	–	–	103.4	0.72	–
1ES 2322-409	6.34 ± 0.13	8.92 ± 0.29	2.5 ± 0.5	50.5	0.83	0.04
1ES 2344+514	10.87 ± 0.22	–	–	250.4	0.73	–
H 2356-309	1.85 ± 0.04	–	–	62.1	0.69	–

Col. (1) Name.

Col. (2) *WISE* flux in the 3.4 $\mu\text{m}$  band.Col. (3) *eROSITA* flux in the 0.2 – 2.3keV band.Col. (4) *eROSITA* flux in the 2 – 5keV band.

Col. (5) The radio flux from SUMSS, NVSS, or FIRST. If the source is found in all 3 catalogs, the NVSS flux is listed, if the source is found in only SUMSS and FIRST, the FIRST flux is listed. If the source is from SUMSS, it is the flux at 843 MHz, otherwise, it is the flux at 1.4 GHz.

Col. (6) The effective spectral index radio to infrared.

Col. (7) The effective spectral index infrared to X-ray as measured with *eROSITA* (not given for sources in the Eastern hemisphere).

**Table A2.** List of *WISE* sources that are discarded as potential TeV candidates due to the *eROSITA* counterpart being flagged as an extended X-ray source in the eRASS1 catalog.

WISEA	eRASS1
J021616.62-481625.9	J021616.7-481624
J024235.93-213225.6	J024235.9-213225
J031757.67-441417.0	J031757.8-441417
J040422.61-651013.0	J040422.7-651016
J043902.25+052043.6	J043902.2+052039
J102557.93+124103.2	J102557.9+124108
J113250.86+142738.6	J113251.1+142739
J114124.20-121638.5	J114124.0-121639
J152412.92-315422.6	J152412.8-315421
J153014.29-423151.7	J153014.1-423147
J180228.51-523645.6	J180228.7-523646
J013803.72-215531.2	J013803.9-215530
J023727.86-263028.7	J023727.6-263031
J051031.94-183844.0	J051031.7-183842
J051636.92+062648.4	J051636.9+062648
J071023.81+224002.4	J071023.8+224004
J073720.91+351741.8	J073721.1+351739
J080056.86+360324.9	J080056.8+360324
J081545.88+100411.4	J081545.8+100407
J083759.97-425926.7	J083759.7-425925
J084255.97+292727.0	J084255.8+292722
J100638.78+255440.8	J100639.0+255443
J104432.88-070406.3	J104432.9-070406
J105036.50-023616.3	J105036.3-023618
J110331.50-083511.1	J110331.3-083513
J111111.17-300922.1	J111111.2-300924
J111450.28-121350.5	J111450.1-121353
J113542.70-202105.8	J113542.4-202109
J121259.25+272704.1	J121259.1+272708
J150722.47-432324.6	J150722.4-432328
J183659.31-664907.7	J183658.7-664905

**Table A3.** List of *WISE* sources that are discarded as potential TeV candidates because a radio counterpart within 5'' is not found.

WISEA	eRASS1
J043509.66-752743.8	J043509.7-752743
J081749.19+025059.3	J081749.1+025058
J051541.41+010440.3	J051541.4+010440
J132838.69+120952.5	J132838.6+120953
J213237.80-623750.9	J213237.9-623750
J135120.21+033716.5	J135120.1+033716
J144909.23-090815.4	J144909.3-090815
J105037.90+170208.3	J105038.1+170209
J033334.62-425552.3	J033334.6-425552
J070819.92-412333.7	J070819.6-412333
J202943.64-552247.9	J202943.8-552245
J030321.79-633820.6	J030321.6-633819
J084853.09+282411.8	J084852.9+282415
J010710.08-321655.0	J010709.8-321654
J014100.48-675327.3	J014100.5-675326
J103946.98-050658.5	J103947.2-050657
J123137.69-493423.9	J123137.7-493424
J101121.18-021239.7	J101121.0-021241